

Proceeding Paper

The Thiadiazole Ring (THD) Is a Building Block for Potential Inhibitors of the SARS-CoV-2 Main Protease (Mpro): Theoretical Look into the Structure, Reactivity, and Binding Profile of Three 1,3,4-THD Derivatives toward Mpro †

Dileep Chikkur Shanthakumar ^{1,*}, Lohith Tumakuru Nagarajappa ^{2,3}, Bienfait Kabuyaya Isamura ^{4,5,6,*}, Mofeli Benedict Leoma ⁷, Kabelo Phuti Mokgopa ⁷, Sridhar Mandayam Anandalwar ^{2,*}, Sahana Doreswamy ⁸ and Srikantamurthy Ningaiah ⁹

¹ Department of Physics, Vidyavardhaka College of Engineering, Visvesvaraya Technological University, Mysuru 570 002, India

² Department of Physics, The National Institute of Engineering (North Campus), Mysuru 570 018, India; lohith@uomphysics.net

³ Department of Studies in Physics, University of Mysore, Mysore 570 006, India

⁴ Department of Chemistry, Faculty of Science, University of Kinshasa, Kinshasa B.P. 190, Democratic Republic of the Congo

⁵ Research Center for Theoretical Chemistry and Physics, Faculty of Science, University of Kinshasa, Kinshasa B.P. 190, Democratic Republic of the Congo

⁶ Department of Chemistry, The University of Manchester, Manchester M13 9PL, UK

⁷ Department of Chemistry, Rhodes University, Makhanda 6140, South Africa; mofedyleoma@gmail.com (M.B.L.); racerpoet1@gmail.com (K.P.M.)

⁸ Department of Physics, Mysore University School of Engineering, Manasagangotri, University of Mysore, Mysore 570 006, India; sahanagowda37@gmail.com

⁹ Department of Chemistry, Vidyavardhaka College of Engineering, Visvesvaraya Technological University, Mysuru 570 002, India; srijmn@vvce.ac.in

* Correspondence: dileepcs@vvce.ac.in (D.C.S.); isamurabft@gmail.com (B.K.I.); mas@physics.uni-mysore.ac.in (S.M.A.)

† Presented at the International Conference on Recent Advances on Science and Engineering, Dubai, United Arab Emirates, 4–5 October 2023.

‡ These authors contributed equally to this work.



Citation: Shanthakumar, D.C.; Nagarajappa, L.T.; Isamura, B.K.; Leoma, M.B.; Mokgopa, K.P.; Anandalwar, S.M.; Doreswamy, S.; Ningaiah, S. The Thiadiazole Ring (THD) Is a Building Block for Potential Inhibitors of the SARS-CoV-2 Main Protease (Mpro): Theoretical Look into the Structure, Reactivity, and Binding Profile of Three 1,3,4-THD Derivatives toward Mpro. *Eng. Proc.* **2023**, *59*, 94. <https://doi.org/10.3390/engproc2023059094>

Academic Editors: Nithesh Naik, Rajiv Selvam, Pavan Hiremath, Suhas Kowshik CS and Ritesh Ramakrishna Bhat

Published: 21 December 2023



Copyright: © 2023 by the authors. Licensee MDPI, Basel, Switzerland. This article is an open access article distributed under the terms and conditions of the Creative Commons Attribution (CC BY) license (<https://creativecommons.org/licenses/by/4.0/>).

Abstract: Thiadiazole (THD) derivatives are famous for their exceptional chemical properties and versatile biological activities. In this work, we report computational investigations of the structure, reactivity, and binding affinity of three 1,3,4-THD derivatives (THDs) toward the SARS-CoV-2 main protease (Mpro). Hirshfeld surface (HS) analyses are carried out in conjunction with topological calculations in the context of the quantum theory of atoms in molecules (QTAIM) and reduced density gradient (RDG) to unravel the nature and magnitude of noncovalent interactions that contribute to maintaining these THDs. The three approaches consistently indicate that the titled THDs are mainly stabilized by weak intramolecular H...H, C-H... π , C-H...N, and N-H...H interactions in their monomeric forms, while their dimers also exhibit intermolecular π ... π stacking and T-shaped contacts. In addition, Hirshfeld atomic charges, frontier molecular orbitals (FMOs), Fukui functions, and molecular electrostatic potential (MEP) reveal that the pyrrolic H atom (ring F) and the imidazole N atom (ring E) are the preferred binding sites for nucleophilic and electrophilic attacks, respectively. Finally, docking and molecular dynamics simulations demonstrate the remarkable binding profile of THDs toward the Mpro, which can be related to potential inhibitory activity.

Keywords: thiadiazole derivatives; Hirshfeld surface; QTAIM; MEP; molecular docking; molecular dynamics

1. Introduction

Thiadiazoles are heterocyclic compounds characterized by the thiadiazole (THD) circle, which is a planar, five-membered, aromatic, and electron-deficient ring comprising one sulfur atom and two pairs of carbon and nitrogen atoms [1]. The thiadiazole (THD) ring exists in four isomeric forms that differ by the relative position of the constituting atoms [2]. Due to their exceptional chemical properties and versatile biological activities, THD-containing compounds have motivated a panoply of excellent experimental investigations over the past decades [3,4]. Taking on a special accent, reported studies on 1,3,4-THD derivatives outstandingly cover their synthesis and assessment of different types of antimicrobial activities [5,6]. For instance, Schenone et al. reported the successful preparation of two novel 1,3,4-THDs endowed with good analgesic and anti-inflammatory activity [7]. Also documented are many examples of 1,3,4-THDs with antituberculosis and antitumor activities.

Besides laboratory experiments, which are often time-consuming, risky, and error-prone, the advent of powerful computers has made it easier to simulate the properties and behavior of molecular systems [8]. Today, chemists resort to various types of computer simulations not only to rationalize or confront their experimental observations but also to make predictions about unseen or challenging systems. For instance, in support of the experimentally approved antitumor and antimicrobial properties of numerous members of the 1,3,4-THDs class, molecular docking studies have demonstrated the ability of these compounds to favorably and spontaneously bind inside the active site of many strategic biomacromolecules that play a prominent role in the life cycle of several microorganisms [9,10]. Moreover, numerous investigations based on QSAR and pharmacophore modeling have undoubtedly proven that the biological activity of drug candidates is mainly determined by their structure and inherent reactivity [11,12]. Therefore, investigating the structure and reactivity of biologically active compounds in general, and that of 1,3,4-THDs, deserves a great deal of attention as this constitutes an important step toward comprehending the origin of their acknowledged activity. Also, of special interest in the current international crisis related to the COVID-19 pandemic would be the assessment of their potential inhibitory activity against crucial proteins of the SARS-CoV-2 virus with the hope to come up with drug candidates for use against COVID-19.

Despite the abundant literature on 1,3,4-THDs, not enough documentation has been reported on the origin of their structural stability, inherent reactivity, and binding affinity to important enzymes of SARS-CoV-2. As an original contribution to this noteworthy challenge, the present study discusses, in an informed tone, the structure, the reactivity, and the binding affinity of three 1,3,4-THDs (general scheme shown in Figure 1), whose crystal structure was laconically reported by Shamanth and coworkers [13–15]. For the sake of clarity, the six rings in compounds 1–3 have been labeled from A to F, with ring D corresponding to the 1,3,4-THD skeleton. Although they share most of their structural features, the titled compounds still differ by either the number and/or the type of substituting halogen atoms inserted in the A and B rings, which was expected to induce local variations.

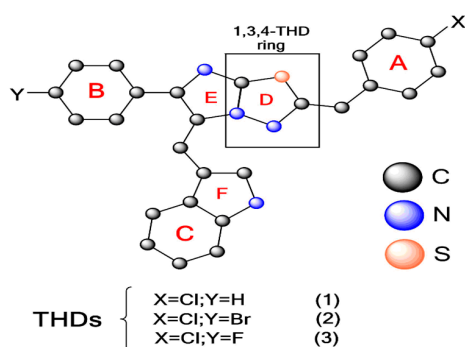


Figure 1. Schematic representation of the four thiadiazole derivatives investigated in this study. Note that H atoms have been omitted from this graph for clarity.

Several state-of-the-art computational techniques are jointly applied to reach the goal assigned to this study. First, the structure of compounds 1–3 is examined via Hirshfeld surface analyses and topological calculations in the context of the quantum theory of atoms in molecules (QTAIM) and the reduced density gradient (RDG) [16]. These same approaches have provided satisfactory results for the elucidation of physical interactions within various molecular frameworks.

2. Methodology

2.1. Density Functional Theory (DFT) Calculations

DFT calculations were performed to understand the inherent chemical reactivity of the three THDs. All the calculations were performed using Gaussian 09 software [17]. Compounds 1–3 were fully optimized using the B3LYP functional in conjunction with the 6-311++G(d,p) basis set. The returned stationary points were confirmed via vibrational frequency calculations to be real minima on the potential energy surface. This level of theory has been shown to provide high-quality results on similar systems [18]. Further, the FMOs, Fukui functions, and MEP maps of the three THDs are visualized via GaussView 6.0 software [19] and Avogadro 1.0 [20].

In addition, based on the electron density distribution, Bader's quantum theory atoms in molecules (QTAIM), and reduced density gradient (RDG)-based noncovalent interaction (NCI) analyses are performed to comprehend the interactions occurring within and between pairs of THDs. The electron density and associated Laplacian, potential, kinetic, and total energy densities at the bond critical points (BCPs) are used to determine the type and strength of interactions in the molecule (BCPs). These topological calculations were carried out using MultiWFN 3.8 software [21] and the results are visualized via Visual Molecular Dynamics 1.9.3 software [22].

2.2. Molecular Docking

To assess the binding affinity of the titled compounds toward the active site of SARS-CoV-2 main protease, Mpro, molecular docking calculations were performed using Autodock Vina [23,24]. Besides considering the optimized B3LYP/6-311++G(d,p) geometries of the ligands for this purpose, the crystal structure of Mpro was retrieved from the protein databank (PDB ID: 6LU7) and its preparation involved, but was not restricted to, the addition of H atoms, the minimization of the protein's energy, and the removal of solvating water molecules and the co-crystallized native ligand. Mpro is a 33.8-kDa homodimer made of 306 amino acids (AA) in each protomer and encloses three functional domains denoted as Domain I, II, and III. The active site, situated between the cleft of domains I and II, was defined as in our recent studies [25,26], while the docking exhaustiveness was fixed at 2000 for better atomic flexibility. Finally, best-docked poses were visualized using BIOAVIA Discovery Studio 3 Visualizer [27].

2.3. Molecular Dynamics Simulation

Umbrella sampling molecular dynamics (MD) simulations were carried out at 298 K and 1 atm in the NPT ensemble using the all-atoms OPLS_2005 force field, as implemented in the Schrodinger 2023-4 package. These simulations were initiated from the best-docked protein-ligand complexes.

3. Results and Discussion

This study explores both the crystal and gas phase geometries of the three THDs to get insight into their structure, chemical reactivity, and binding profile toward the Mpro (Figure 2).

For the sake of concision, this section is sequenced into six paragraphs. In Section 3.1, the crystal structures of the three THDs in their monomeric and dimeric forms are scrutinized based on Hirshfeld surface (HS).

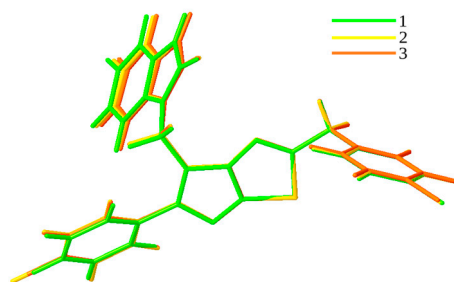


Figure 2. Superimposition of DFT-optimized structures of the three THDs.

3.1. QTAIM and RDG Analyses for Dimers

To extend the study on noncovalent interactions present in the crystal structures of the three THDs, single-point energy calculations were performed on the dimers to extract the associated density and realize QTAIM and RDG analyses. The details of various noncovalent interactions observed in compounds 1–3 are summarized in Table 1 and shown in Figure 3.

Table 1. QTAIM-analysis of the dimers of the three THDs. B3LYP/6-31++G(d,p) wave function extracted from the crystal structure.

	BCP	ρ_{BCP} (a.u.)	$\nabla^2\rho$ (a.u.)	$V(r)$ (a.u.)	$G(r)$ (a.u.)	$\frac{-G(r)}{V(r)}$	λ_1	λ_2	λ_3	$\frac{ \lambda_1 }{\lambda_3}$	E_{HB} (kcal/mL)
1	113	0.0023	0.0065	−0.0009	0.00128	1.422	−0.0012	−0.0004	0.0078	0.153	−0.229
	136	0.0076	0.0362	−0.0040	0.00656	1.64	−0.0047	−0.0035	0.0445	1.056	−0.953
	189	0.0207	0.0669	−0.0150	0.0158	1.053	−0.025	−0.0233	0.115	0.217	−3.875
	191	0.0057	0.0193	−0.0025	0.0036	1.44	−0.0034	−0.0032	0.026	0.130	−0.529
	197	0.0005	0.0017	−0.00018	0.0003	1.666	−0.0002	−0.0001	0.00216	0.009	−0.630
2	152	0.00220	0.0067	−0.00089	0.00128	1.438	−0.0012	−0.0008	0.00882	0.136	−0.251
	137	0.00383	0.0100	−0.0017	0.00214	1.258	−0.0018	−0.0004	0.0123	0.146	−0.112
	189	0.0062	0.0222	−0.00355	0.00455	1.281	−0.0048	−0.0017	0.0288	0.166	−0.640
	207	0.00319	0.0093	−0.00128	0.00181	1.414	−0.0018	−0.0012	0.0125	0.144	−0.003
	175	0.0086	0.0373	−0.0045	−0.00692	1.537	−0.0072	−0.0052	0.0497	0.144	−1.176
3	150	0.0079	0.0382	−0.0043	0.0069	1.604	−0.0042	−0.0028	0.0453	0.09	−1.02
	224	−0.0040	0.0100	−0.0016	0.0020	1.25	−0.0018	−0.0009	0.0127	0.142	−0.150
	178	0.0068	−0.0227	−0.0036	0.0046	1.277	−0.0062	−0.0056	0.0346	0.179	−0.774
	131	0.0040	0.0099	−0.00168	0.0020	1.190	−0.0018	−0.0010	0.0127	0.141	−0.150

As can be seen from Figure 3, various noncovalent interactions like C-H... π , π ... π , H...H, and N-H...N interactions are responsible for the packing of the dimers. In dimer 1, ring A and rings C and F are involved in π ... π stacking interactions which are evidenced by the BCPs 113 and 112, and validated by the appearance of green isosurfaces (encircled by the black color) between said rings. In addition, the N-H...N intermolecular interaction is observed in the crystal packing of the compound-1 which is observed in the Hirshfeld surface analysis. In dimer 2, numerous interactions like C-H... π , C-H...N, and C-H...Br are confirmed by the presence of BCPs 248, 189, and 207 (which also validates the C-H...Br interaction's existence in the Hirshfeld surface analysis). Noteworthy is the presence of a π ... π T-shaped substructure in dimer 2 which is favored by the formation of BCPs 152 and 137. This π ... π T-shaped region is unique to dimer 2 and does not appear in either dimer 1 or 3, which are rather characterized by the presence of 1 and 2 π ... π stacking contacts, respectively. Furthermore, dimer 3 stands out for presenting an inversion center. It also

carries C-H...N intermolecular interactions which are responsible for the supramolecular synthon validated by the BCPs 178 and 176 and encircled in the RDG image. Finally, like intramolecular contacts in the monomers, the intermolecular interactions in the dimeric forms of compounds 1–3 are very weak, as suggested by the individual EHB values. The most pronounced is the N...H hydrogen bond (BCP 189) observed in dimer 1, with an estimated EHB value of roughly -3.9 kcal/mol.

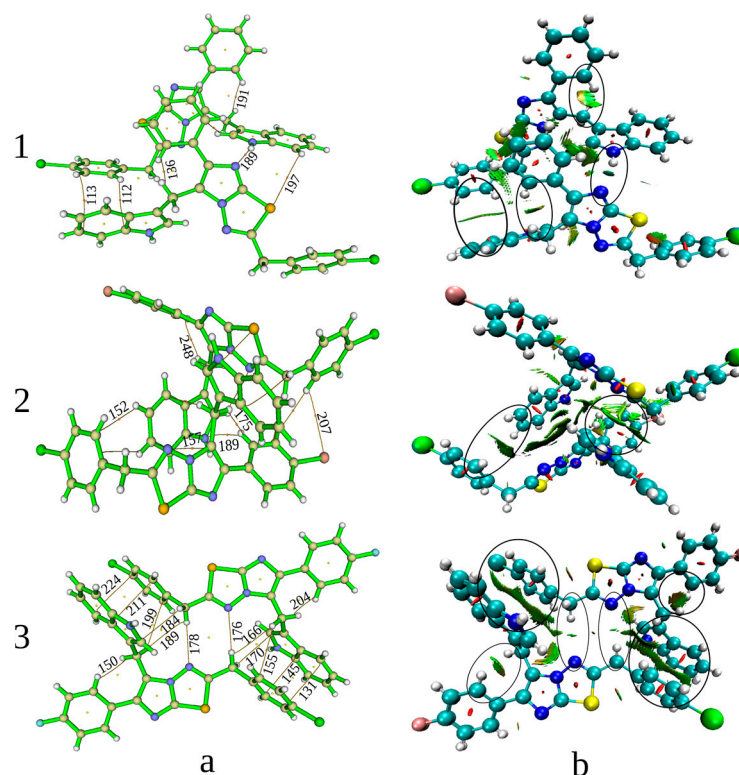


Figure 3. (a) QTAIM; (b) RDG analyses for the dimers of three compounds 1–3.

3.2. Chemical Reactivity

Chemical reactivity is one of the most documented topics in the computational chemistry community [28–30]. After years of dedicated research, several mathematical tools have been proposed to assess the reactivity of chemicals. These reactivity descriptors are often categorized into local and global indicators. The concept of local descriptors applies to any reactivity indicator that can be used to predict the most reactive sites within a given molecule, while global descriptors are parameters that probe the entire system to provide an overall estimation of its reactivity [31]. Among the most employed local descriptors are the atomic charges, frontier molecular orbitals, molecular electrostatic potentials, and Fukui functions. On the other hand, global descriptors are often well-suited when it comes to establishing reactivity trends within a series of compounds. In this vein, conceptual DFT (CDFT) is a broad reactivity paradigm that offers the means to evaluate the global reactivity of chemicals based on the quantification of the response of chemicals to various perturbations. The mathematical foundations of CDFT are provided elsewhere [32]. For a more comprehensive conclusion on the reactivity of the three THDs, we herein rely on all of the aforementioned descriptors.

(a) Frontier molecular orbitals

Frontier molecular orbitals (FMOs), i.e., the highest occupied molecular orbital (HOMO) and the unoccupied molecular orbital (LUMO), are extensively relied on to assess the reactivity of molecular systems. Indeed, it is well known that kinetic stability, which inversely correlates with chemical reactivity, can be predicted based on the energetic gap between the HOMO and LUMO. A rule of thumb is that the larger the gap, the less reactive the

compound is, and vice versa. On the other hand, it is believed that much of the local reactivity of a compound is hidden inside the electron density distribution of the HOMO and LUMO, which, respectively, relate to the ionization potential and electron affinity. Figure 4 displays the HOMO and LUMO of the three THDs, their energies, and the gap between them.

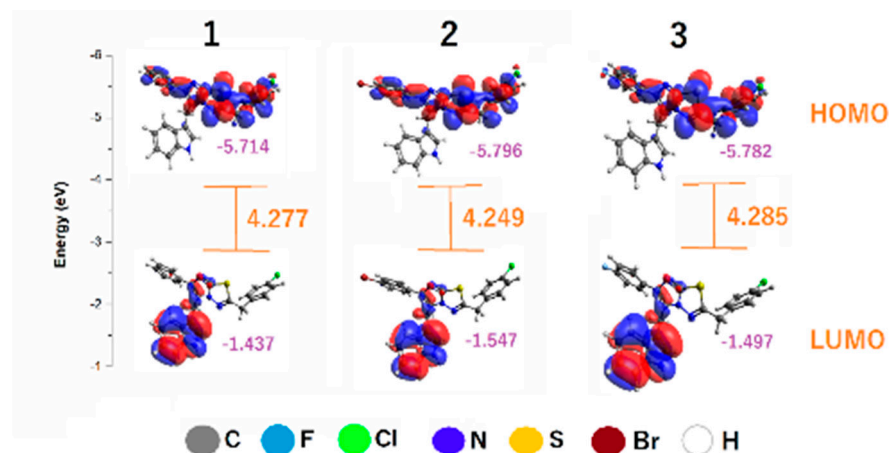


Figure 4. HOMO and LUMO orbitals of compounds 1–3 at the B3LYP/6-311++G(d,p) level.

Looking at the HOMO-LUMO gaps in Figure 4, it comes out that compound 2 is slightly more reactive or less kinetically stable than its analogs, 1 and 3. Furthermore, Figure 4 indicates that compounds 1–3 share most of their local reactivity features. Regardless of the compounds, the HOMO is concentrated on rings C, E, and F, while the LUMO spreads over rings A, B, E, and D. As such, the clouds of rings C and F constitute good binding sites for electrophilic species, while sites on rings A, B, and D are grossly electron-deficient and might get involved in interactions with nucleophilic entities. Ring E seems to be amphoteric as it contributes to the stability of both the HOMOs and LUMOs. However, note that, although it contributes to the stability of the HOMO, ring F carries the most electrophilic local site, i.e., the pyrrolic H atom, as suggested by the atomic charges and MEPs (next paragraph).

(b) Molecular electrostatic potential (MEP)

The MEP is one of the most employed local reactivity descriptors for the elucidation of regioselectivity [33]. Assuming the validity of the Born–Oppenheimer approximation, the electrostatic potential $V(r)$ at a given point r of a molecular surface is calculated using Equation (3), $V(r) = \sum_{A=1}^M \frac{Z_A}{|R_A-r|} - \int \frac{\delta\rho(r)}{|r-r'|}$ where Z_A is the nuclear charge at position A , $\rho(r)$ is the electron density of the system at point r , and M is the number of nuclei in the system [33]. On the MEP, red and blue regions correspond to negative and positive electrostatic potentials (ESP), respectively.

Figure 5 depicts the MEP maps of compounds 1–3 at the 0.001 isosurface. Also exhibiting a positive ESP are the positively charged H atoms attached to all the rings. Regarding the halogen atoms, it is interesting to note that, in the three 1,3,4-THDs, the chlorine atom is always endowed with a σ -hole in the axis of the Cl–C (ring A) bond. A distinctive feature between compounds 2 and 3 is that the bromine atom in 2 bears a very pronounced sigma hole, while the fluorine atom in 3 has a negative ESP. This finding can be explained by the large difference in electronegativity between F and Br. Based on this, the Br and Cl atoms should be favorable for electrophilic attacks along the C–Cl and C–Br axes, while the F atom would prefer nucleophilic antagonists.

Although the MEP maps in Figure 5 clearly distinguish local sites in terms of their electronic character, they are restricted to providing a qualitative picture of the local reactivity, which unfortunately does not inform on the most reactive sites. To respond to this further pertinent question, the topology of the MEP function was examined at the

0.001 isosurface. This allowed us to discriminate between the different sites and appreciate the extent of the holes on the Cl and Br atoms.

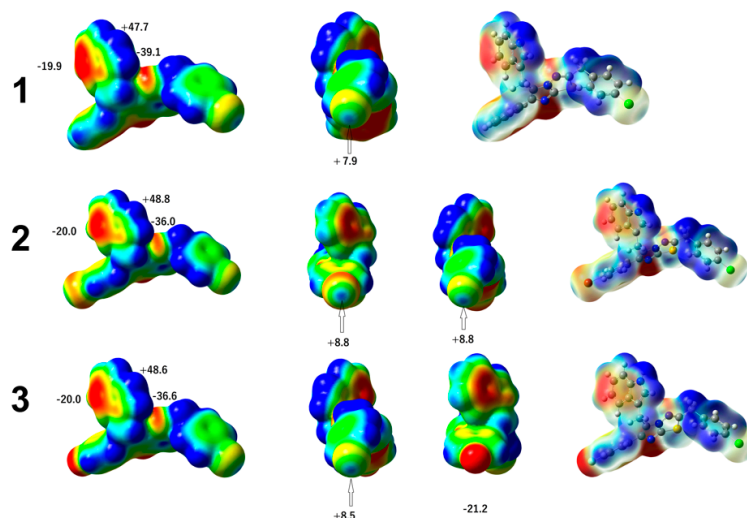


Figure 5. Molecular electrostatic potential (MEP) maps of compounds 1–3 generated at the 0.001 isosurface.

To begin with, note that the topology of the MEP function presents several maximum and minimum values, but only the most relevant retained our attention. First, the global minimum was found in the vicinity of the imidazole N atom (ring E) and was estimated at -39.1 , -36.0 , and -36.6 kcal/mol for compounds 1–3, respectively. This spot is therefore the most nucleophilic site and corroborates with atomic Hirshfeld charges. On the other hand, the global maximum, i.e., 47.7 , 48.8 , and 48.6 kcal/mol, is associated with the pyrrolic H atom of ring F in compounds 1–3, respectively. This observation is once more consistent with atomic charges. The topology of the MEP also shows that the two sides of rings C and A constitute distinct reactive sites. For instance, ring E of compound 1 has two ESP minima of -21.6 and -21.3 kcal/mol at the two faces, which indicates that the first face is slightly more nucleophilic than the second one. The same qualitative conclusion applies to compounds 2 and 3. Moreover, the lone pairs of the Cl atom are well detected by the presence of local ESP minima around the atom. In compound 2, for instance, these local ESP minima are equal to -8.9 and -9.7 kcal/mol. Moreover, the negative ESP on F in compound 3 is well reflected by three local extrema estimated at -21.5 , -21.6 , and -20.4 kcal/mol, i.e., an average local ESP of -21.2 kcal/mol (as indicated in Figure 5). Finally, regarding σ -holes, the one on the Cl atom is linked to an ESP local minimum of 7.9 , 8.8 , and 8.5 kcal/mol in compound 1–3, respectively, against an 8.8 kcal/mol ESP σ -hole for the bromine atom in compound 2. This proves that the σ -holes created on the Cl and Br are of similar deepness; though, the presence of the second halogen atom in the molecule seems to enhance the extent of the σ -hole on the Cl atom.

(c) Global reactivity

Table 2 collects global reactivity descriptors of compounds 1–3 calculated in the framework of the CDFT. These descriptors suggest that compounds 1–3 are of similar reactivity, with their slight differences mostly lying within the limit of the accuracy of the density functional theory. Despite their outstanding similarity, one can carefully make some comments on their slight reactivity deviations among the three THDs. For instance, chemical hardness measures how resistant a molecule is to the distortion of its electron density, while the softness S has the exact opposite meaning. Based on this, it comes from Table 2 that compound 2 is slightly more polarizable than the two others, with an S value of 0.471 eV, as compared with the 0.468 and 0.467 eV obtained for compounds 1 and 3, respectively. The same table also predicts compound 2 as the most electrophilic and should therefore develop the strongest interactions with electron-rich species. This finding corroborates with the topology of the MEP, which showed that the global ESP maximum

of compound 2, i.e., 48.8 kcal/mol, is slightly higher than those of compound 1 and 3, i.e., 47.5 and 48.6 kcal/mol, respectively. Moreover, ionization potentials and electron affinities follow the same pattern, namely compound 1 < compound 3 < compound 2. As expected, this suggests that the amount of energy required to produce mono-ionized species from the neutral compounds 1–3 increases with the number and size of the halogen atoms present in the titled compounds.

Table 2. CDFT reactivity descriptors of compounds 1–3 at the B3LYP/6-311++G(d,p) level.

Compounds	IP	EA	η	S	μ	ω
1	5.714	1.438	2.138	0.468	−3.576	2.990
2	5.796	1.547	2.125	0.471	−3.672	3.172
3	5.782	1.497	2.143	0.467	−3.639	3.091

3.3. Binding Affinity of Compounds 1–3 toward Mpro

Among important proteins of the SARS-CoV-2 virus, the main protease (Mpro) is involved in the processing of polyproteins into functional proteins, which constitutes a crucial step in the replication of the virus. It is expected that effective inhibitors of this enzyme should mitigate the proliferation of infectious viral particles and subsequently alleviate COVID-19 symptoms [34]. Therefore, the Mpro (Figure 6) has become one of the most attractive targets for the design of potential drugs against SARS-CoV-2.

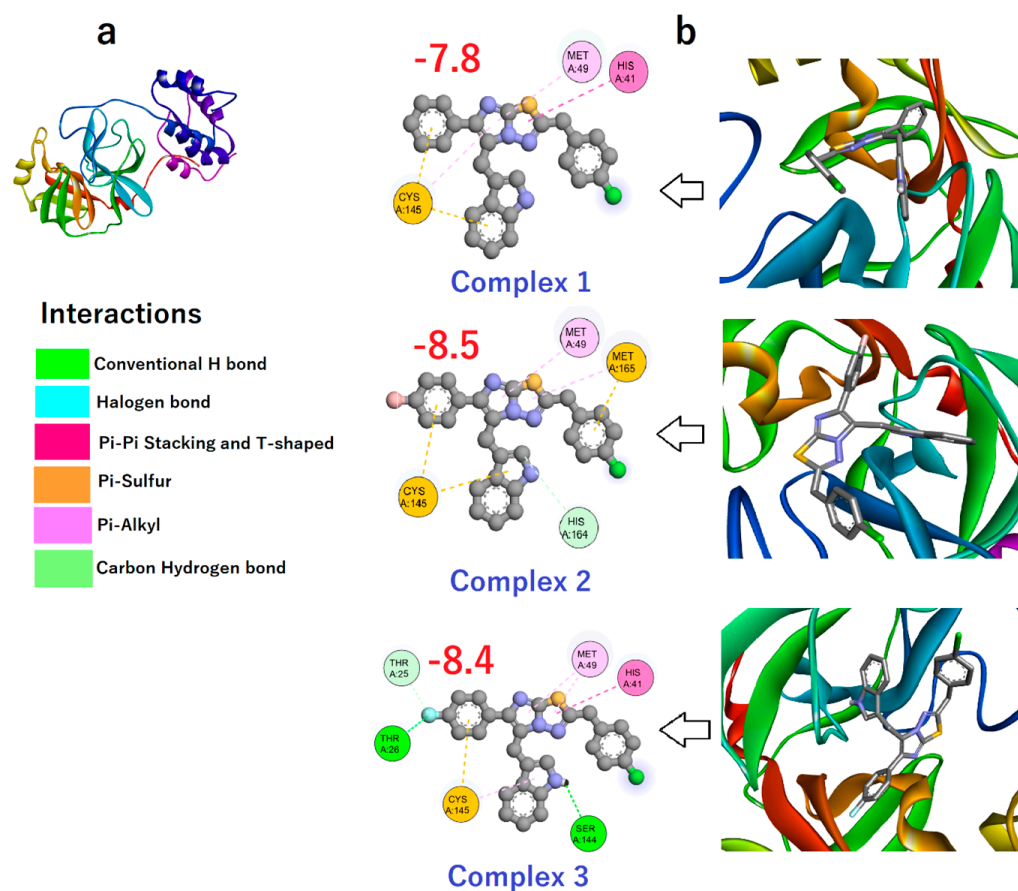


Figure 6. (a) 3D structure of Mpro protomer; (b) best docked poses and 2D interaction diagrams of all protein–ligand complexes. All physical interactions between ligands and residues in the active site of Mpro are indicated in the legend. Binding energies (in red) are expressed in kcal/mol.

Several strategies, of which the most popular are the drug repurposing of FDA-validated antivirals and the virtual screening of online libraries [35], have been attempted to identify promising candidates against the Mpro which can inhibit the activity of the Mpro. While the two previous approaches rely on existing molecules, another promising avenue consists of synthesizing new molecules and testing their potential inhibitory activity against the Mpro [36]. Following the same rationale, we have assessed the binding mode of the titled compounds inside the active site of the Mpro via docking calculations.

Figure 6b displays the best-docked poses and 2D interaction diagrams of all ligand-protein complexes. Predicted binding energies fall within the range of -7.8 to -8.5 kcal/mol, which suggests an overall favorable and spontaneous packing of the ligands inside the active site of the Mpro. The THD candidates have slightly higher binding energies compared with the co-crystallized native ligand (i.e., -6.8 kcal/mol using Autodock Vina), which often serves as a positive control [37,38]. This suggests that the three candidates are likely to possess inhibitory activity. This finding is consistent with the widely approved antimicrobial properties of THD-containing molecular frameworks.

Moreover, close inspection of the best-docked poses revealed that protein-ligand complexes are stabilized by several types of noncovalent interactions, the most noteworthy being hydrogen bonds, halogen bonds, and $\pi \dots S$ and $\pi \dots \pi$ contacts. Two residues are almost omnipresent in interactions of the Mpro and compounds 1–3, i.e., CYS145 and HIS41. These AAs are important constituents of the active site of the Mpro enzyme and appear, respectively, in the functional domains I and II of the catalytic dyad of each Mpro protomer [39]. The presence of two lone pairs on the sulfur atom of CYS154 allows it to establish two spatially distinct $\pi \dots S$ contacts with the electronic cloud of ring B (complexes 1–3) and either of the rings C (complex 1) or F (complex 2–3). On the other hand, HIS41 develops $\pi \dots \pi$ interactions with the thiadiazole ring D in complexes 1 and 3. Depending on the relative orientation of the imidazole (HIS41) and thiadiazole (compound 1 and 3) rings, one could differentiate two types of $\pi \dots \pi$ contacts, corresponding to the so-called stacking and T-shaped interactions. In the first case, the two rings are parallel to each other, while in the latter situation, they are positioned perpendicularly to each other. Other important residues of the active site include THR26 and SER144. The first amino acid residue is engaged in a halogen bonding interaction with the fluorine atom of compound 3, while the latter forms a hydrogen bond with the pyrrolic H atom of ring F.

In light of the previous docking results, the three compounds present interesting binding profiles to the Mpro and might be regarded as potential inhibitors of this enzyme. However, it has to be emphasized that the Mpro is not the only current target for potential antiviral drugs against SARS-CoV-2. Another widely admitted target for the design of CoVID-19 drug candidates is the papain-like protease Plpro, which, similarly to the Mpro, is also essential to the regulation of the virus' spread and innate immunity [40]. Also being targeted today is the spike glycoprotein of SARS-CoV-2 (S-protein) which mediates the access of the virus into the host cell [41].

3.4. Molecular Dynamics Simulation

Molecular docking calculations alone are never conclusive. A very common practice to confirm the affinity of the ligand toward a target consists of performing post-docking analyses, such as molecular dynamics (MD) simulations. In the present study, MD simulations were performed on protein-ligand complexes to understand their dynamics over some time of 100 ns [42–45]. The fluctuations of the protein and ligands throughout the simulation are summarized by the RMSD plots shown in Figure 7a. The RMSD of the ligand is obtained by aligning the protein-ligand complex on the protein backbone of reference and corresponding to contributions of heavy atoms.

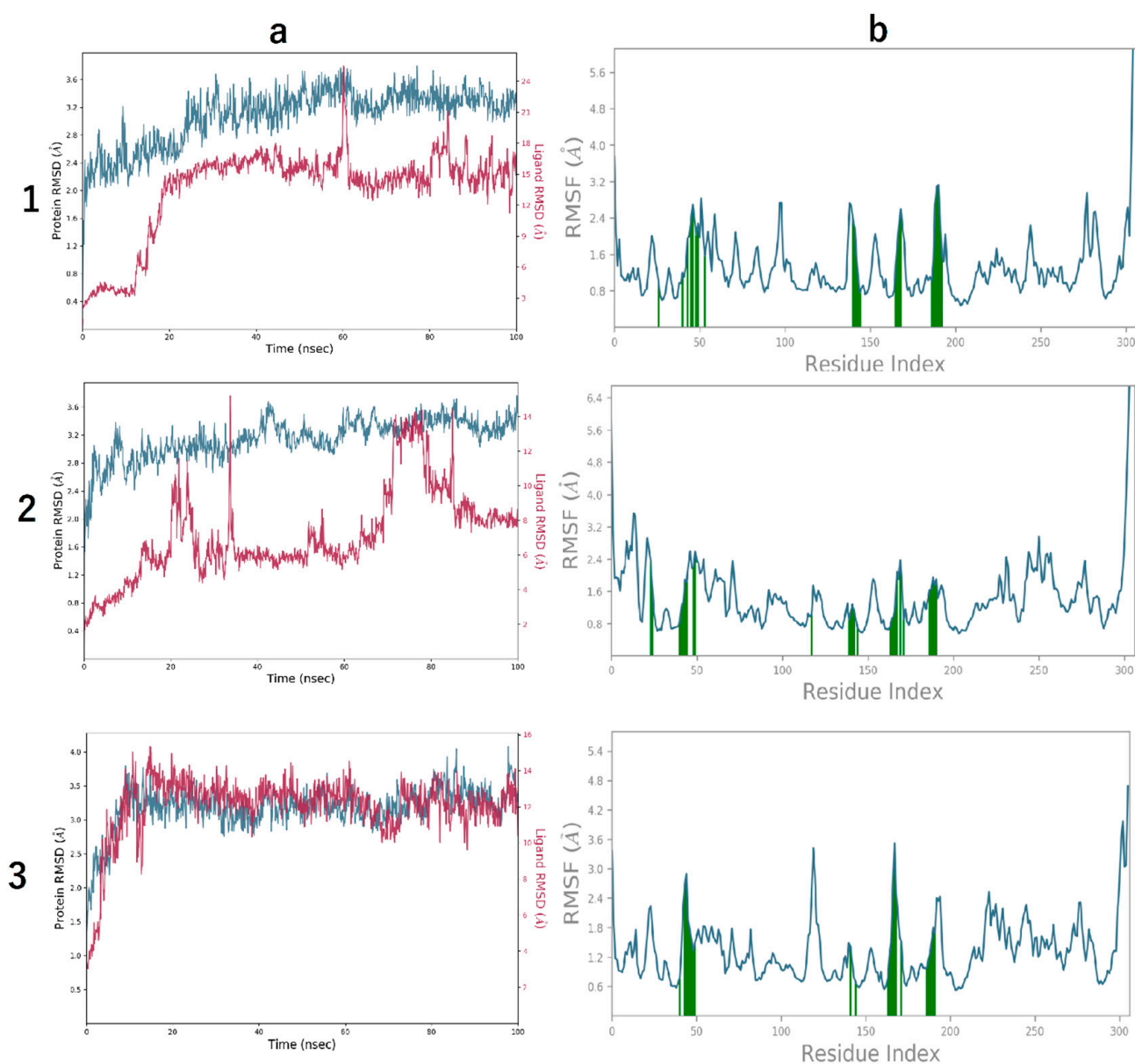


Figure 7. MD simulations of protein-ligand complexes involving Mpro and each of compounds 1–3. (a) RMSD and (b) protein's RMSF.

Figure 7a reveals that in complex 1, the receptor assumes a partial equilibration between 2 and 20 ns, where its RMSD varies from 2.0 to 3.0 Å, while effective equilibration happens after 25 ns, after which the RMSD oscillates between 3.0 and 3.6 Å. The dynamics of the ligand (1) inside the receptor pocket are very latent for the first 12 ns, then it enters a very perturbed period which continues up until its first stabilization around 20 ns. For the next 40 ns, the ligand is relatively cooled down, but this intermediate state changes around the 60th ns when it suddenly jumps. This moment coincides with the cleavage of some pertinent noncovalent interactions, going from four to one protein-ligand contacts before increasing to three around 80 ns. Further, the ligand equilibrates all over the remaining period. In complex 2, the protein equilibrates around the 20th ns, from which time its RMSD slightly fluctuates up to 0.6 Å. The ligand is still very dynamic until the 85th ns, after which it equilibrates. In complex 3, the protein equilibrates after 15 ns, and so does the ligand, but after a sudden structural rearrangement in the sense that reduces the RMSD from 4.0 to 2.2 Å before it rises again and stabilizes around 3.5 Å. The protein RMSD at equilibration is roughly 3.2 Å and oscillates in a range of 0.8 Å for the rest of the simulation. Close

inspection of Figure 7b reveals that, for the three complexes, the protein's root mean square fluctuation (RMSF) is the highest for the N- and C-terminals, as expected. In addition, the protein's RMSF is estimated to be 2.0Å on average, which proves its stability throughout the simulation.

The number of contacts established between the protein and the ligands is one of the main factors that correlate with the dynamics of protein-ligand complexes. Note that some residues form more than one contact with the ligand. Complex 1 is initially stabilized by four noncovalent interactions, but this number fluctuates over the simulation (zero and seven contacts). At the end of the simulation, ligand 1 is still forming three contacts with the Mpro, and these involve SER46, LEU50, and PRO168. PRO168 and LEU50 mostly form hydrophobic bonds and water bridges, while SER46 engages with hydrogen bonding contacts and water bridges (see Figure 8). Regarding the contributions to protein-ligand interactions, GLU189 has the most pronounced contribution (~30%), followed, respectively, by MET19 (~25%), PRO168 (~25%), ALA191 (~23%), and LEU167 (~20%). Protein-ligand complex 2 is stabilized by up to 9 contacts during the simulation time. HIS41 has the highest contribution, occurring in contacts for about ~55% of the simulation time. These contacts include hydrophobic interactions (dominant), H-bonds, and water bridges. Other important residues include PRO168 (~40%), ASN142 (~30%) and GLU166 (~30%). Finally, compound 3 develops four to six contacts with the Mpro in the early steps of the dynamics, and this number varies between zero and five all over the simulation. Throughout the simulation, amino acid residues like ASN142, CYS145, and HIS164 only establish hydrogen bonds with the ligand, while MET49, LEU50, MET165, and ALA191 only occur in hydrophobic interactions. The rest of the contacts involve residues that, in addition to attaching to the ligand, also bind to water molecules. LEU167 has the highest contributions (~48% of the simulation time) to protein-ligand interactions, which are decomposed into hydrophobic contacts and water bridges.

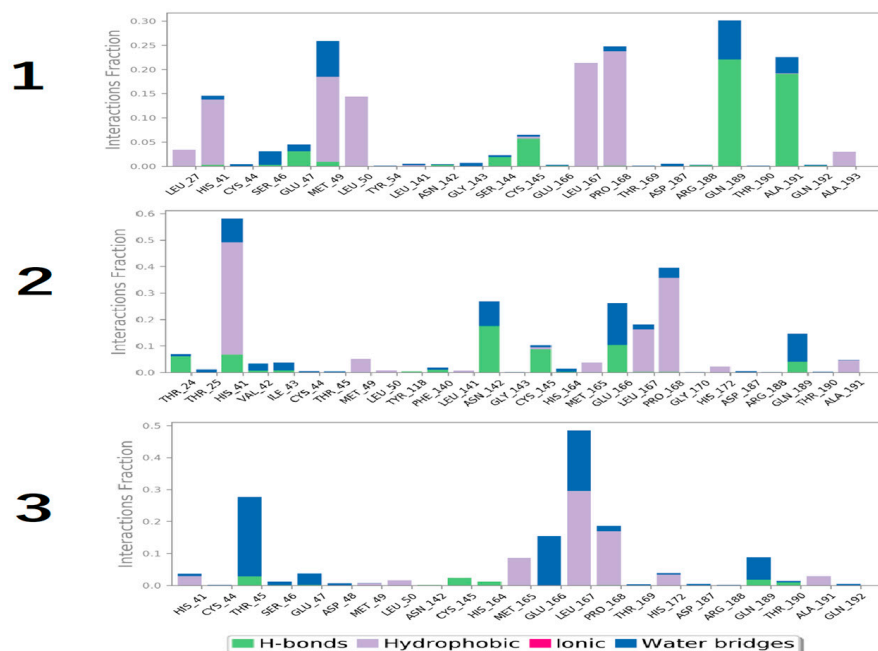


Figure 8. Contributions of residues to the total interactions involving the amino acids in the active site of Mpro and the ligand and water molecules.

4. Conclusions

In this study, we have investigated the structure, reactivity, and binding profile of three 1,3,4-THD derivatives inside the active site of the SARS-CoV-2 main protease (Mpro). Our computations suggest that these compounds are mainly stabilized by the weak H...H and C-H...N noncovalent interactions, while their crystalline dimers also exhibit π ... π stacking

and T-shaped interactions between pairs of aromatic rings. Furthermore, reactivity studies indicate that compounds 1–3 are of similar global reactivity, with their slight differences lying within the limit of the accuracy of the density functional theory. Based on predictions of different local reactivity descriptors, the pyrrolic H atom of ring F and the N atom of ring E are, respectively, pointed to as the best binding sites for nucleophilic and electrophilic antagonists. Finally, docking and MD simulations indicate that the three compounds spontaneously attach to the active site of the Mpro with a binding energy between -7.8 to -8.5 kcal/mol, and are relatively well retained in the active site of the Mpro during the simulation time.

Author Contributions: Conceptualization, L.T.N., B.K.I. and D.C.S.; methodology, D.C.S.; software, L.T.N. and B.K.I.; validation, M.B.L., K.P.M., D.C.S. and L.T.N.; formal analysis, S.D.; investigation, S.N.; resources, B.K.I.; data curation, L.T.N.; writing—original draft preparation, L.T.N. and B.K.I.; writing—review and editing, S.D.; visualization, S.N.; supervision, S.M.A.; project administration, S.M.A.; funding acquisition, D.C.S. All authors have read and agreed to the published version of the manuscript.

Funding: This research received no external funding.

Institutional Review Board Statement: Not applicable.

Informed Consent Statement: Not applicable.

Data Availability Statement: Data are contained within the article.

Acknowledgments: Dileep C S. would like to thank the management and principal of Vidyavardhaka College of Engineering for financial support. BKI is indebted to the BEBUC scholarship program for financial support. MBL and KPM are grateful to the National Research Foundation for postgraduate scholarships. The authors are grateful to Kevin Lobb and the Center for High-Performance Computing for having provided some of the resources used to carry out this study.

Conflicts of Interest: The authors declare no conflict of interest.

References

1. Fouda, A.S.; Heakal, F.E.; Radwan, M.S. Role of some thiadiazole derivatives as inhibitors for the corrosion of C-steel in 1 M H_2SO_4 . *J. Appl. Electrochem.* **2009**, *39*, 391–402. [[CrossRef](#)]
2. Li, Y.; Geng, J.; Liu, Y.; Yu, S.; Zhao, G. Thiadiazole—a Promising Structure in Medicinal Chemistry. *ChemMedChem* **2013**, *8*, 27–41. [[CrossRef](#)] [[PubMed](#)]
3. Amir, M.; Kumar, H.; Javed, S.A. Non-carboxylic Analogues of Naproxen: Design, Synthesis and Pharmacological Evaluation of some 1,3,4-oxadiazole/thiadiazole and 1,2,4-thiadiazole derivatives. *Arch. Pharm. Chem. Life Sci.* **2007**, *340*, 557–585. [[CrossRef](#)] [[PubMed](#)]
4. Szeliga, M. Thiadiazole derivatives as anticancer agents. *Pharmacol. Rep.* **2020**, *72*, 1079–1100. [[CrossRef](#)] [[PubMed](#)]
5. Pal, D.; Tripathi, R.; Pandey, D.; Mishra, P. Synthesis, characterization, antimicrobial, and pharmacological evaluation of some 2, 5-disubstituted sulfonyl amino 1,3,4-oxadiazole and 2-amino-disubstituted 1,3,4-thiadiazole derivatives. *J. Adv. Pharm. Technol. Res.* **2014**, *5*, 196–201. [[CrossRef](#)] [[PubMed](#)]
6. Shawali, A.S. 1,3,4-Thiadiazoles of pharmacological interest: Recent trends in their synthesis via tandem 1,3-dipolar cycloaddition: Review. *J. Adv. Res.* **2014**, *5*, 1–17. [[CrossRef](#)] [[PubMed](#)]
7. Schenone, S.; Brullo, C.; Bruno, O.; Bondavalli, F.; Ranise, A.; Filippelli, W.; Rinaldi, B.; Capuano, A.; Falcone, G. New 1,3,4-thiadiazole derivatives endowed with analgesic and anti-inflammatory activities. *Bioorganic. Med. Chem.* **2006**, *14*, 1698–1705. [[CrossRef](#)] [[PubMed](#)]
8. Kolavi, G.; Hegde, V.; Khazi, I.A.; Gadad, P. Synthesis and evaluation of antitubercular activity of imidazo[2,1-b,1,3, 4]thiadiazole derivatives. *Bioorganic. Med. Chem.* **2006**, *14*, 3069–3080. [[CrossRef](#)]
9. Sun, J.; Yang, Y.S.; Li, W.; Zhang, Y.B.; Wang, X.L.; Tang, J.F.; Zhu, H.L. Synthesis, biological evaluation and molecular docking studies of 1,3,4-thiadiazole derivatives containing 1,4-benzodioxan as potential antitumor agents. *Bioorganic Med. Chem. Lett.* **2011**, *21*, 6116–6121. [[CrossRef](#)]
10. Grimme, S.; Schreiner, P.R. Computational Chemistry: The Fate of Current Methods and Future Challenges. *Angew. Chemie—Int. Ed.* **2018**, *57*, 4170–4176. [[CrossRef](#)]
11. Abdel-Hamid, M.K.; Abdel-Hafez, A.A.; El-Koussi, N.A.; Mahfouz, N.M.; Innocenti, A.; Supuran, C.T. Design, synthesis, and docking studies of new 1,3,4-thiadiazole-2-thione derivatives with carbonic anhydrase inhibitory activity. *Bioorganic Med. Chem.* **2007**, *15*, 6975–6984. [[CrossRef](#)] [[PubMed](#)]

12. Rastija, V.; Medić-Šarić, M. QSAR study of antioxidant activity of wine polyphenols. *Eur. J. Med. Chem.* **2009**, *44*, 400–408. [[CrossRef](#)] [[PubMed](#)]
13. Shamanth, S.; Mantelingu, K.; Kumar, H.K.; Yathirajan, H.S.; Foro, S.; Glidewell, C. Crystal structures of three 6-aryl-2-(4-chlorobenzyl)-5-[(1H-indol-3-yl)methyl]imidazo[2,1-b,1,3,4]thiadiazoles Shamanth Sadashivamurthy. *Acta Crystallogr. Sect. E Crystallogr. Commun.* **2020**, *76*, 18–24. [[CrossRef](#)] [[PubMed](#)]
14. Spackman, M.A.; Jayatilaka, D. Hirshfeld surface analysis. *CrystEngComm* **2009**, *11*, 19–32. [[CrossRef](#)]
15. Nkungli, N.K.; Ghogomu, J.N. Theoretical analysis of the binding of iron(III) protoporphyrin IX to 4-methoxyacetophenone thiosemicarbazone via DFT-D3, MEP, QTAIM, NCI, ELF, and LOL studies. *J. Mol. Model.* **2017**, *23*, 200. [[CrossRef](#)] [[PubMed](#)]
16. Saleh, G.; Gatti, C.; Presti, L.L.; Garcia, J.C. Revealing Non-covalent Interactions in Molecular Crystals through Their Experimental Electron Densities. *Chem.—Eur. J.* **2012**, *18*, 15523–15536. [[CrossRef](#)]
17. Frisch, M.J.; Trucks, G.W.; Schlegel, H.B.; Scuseria, G.E.; Robb, M.A.; Cheeseman, J.R.; Scalmani, G.; Barone, V.; Mennucci, B.; Petersson, G.A.; et al. Gaussian 09 (C.01) Inc., Wallingford, CT, USA. 2009. Available online: <https://gaussian.com/> (accessed on 1 December 2023).
18. Wazzan, N.A.; Obot, I.B.; Kaya, S. Theoretical modeling and molecular level insights into the corrosion inhibition activity of 2-amino-1,3,4-thiadiazole and its 5-alkyl derivatives. *J. Mol. Liq.* **2016**, *221*, 579–602. [[CrossRef](#)]
19. Dennington, J.M.M.R.; Keith, T.A. *GaussView*, version 6.0. 16; Semichem Inc.: Shawnee Mission, KS, USA, 2016.
20. Hanwell, M.D.; Curtis, D.E.; Loni, D.C.; Vandermeersch, T.; Zurek, E.; Hutchison, G.R. Avogadro: An advanced semantic chemical editor, visualization, and analysis platform. *J. Cheminform.* **2012**, *4*, 17. [[CrossRef](#)]
21. Lu, T.; Chen, F. Multiwfn: A multifunctional wavefunction analyzer. *J. Comput. Chem.* **2012**, *33*, 580–592. [[CrossRef](#)]
22. Humphrey, W.; Dalke, A.; Schulten, K. VMD: Visual Molecular Dynamics. *J. Mol. Graph.* **1996**, *14*, 33–38. [[CrossRef](#)]
23. Sandeep, G.; Nagasree, K.P.; Hanisha, M.; Kumar, M.M.K. AUDocker LE: A GUI for virtual screening with AUTODOCK Vina. *BMC Res. Notes* **2011**, *4*, 3–6. [[CrossRef](#)] [[PubMed](#)]
24. Castro-Alvarez, A.; Costa, A.M.; Vilarrasa, J. The Performance of several docking programs at reproducing protein-macrolide-like crystal structures. *Molecules* **2017**, *22*, 136. [[CrossRef](#)]
25. Matondo, A.; Dendera, W.; Isamura, B.K.; Ngbolua, K.; Mambo, H.V.S.; Muzomwe, M.; Mudogo, V. In silico Drug Repurposing of Anticancer Drug 5-FU and Analogues Against SARS-CoV-2 Main Protease: Molecular Docking, Molecular Dynamics Simulation, Pharmacokinetics and Chemical Reactivity Studies. *Adv. Appl. Bioinform. Chem.* **2022**, *15*, 59–77. [[CrossRef](#)] [[PubMed](#)]
26. Alfaro, M.; Alfaro, I.; Angel, C. Identification of potential inhibitors of SARS-CoV-2 papain-like protease from tropane alkaloids from *Schizanthus porrigens*: A molecular docking study. *Chem. Phys. Lett.* **2020**, *761*, 138068. [[CrossRef](#)] [[PubMed](#)]
27. Shivakumar, D.; Harder, E.; Damm, W.; Friesner, R.A.; Sherman, W. Improving the prediction of absolute solvation free energies using the next generation opls force field. *J. Chem. Theory Comput.* **2012**, *8*, 2553–2558. [[CrossRef](#)] [[PubMed](#)]
28. Czeleń, P. Inhibition mechanism of CDK-2 and GSK-3 β by a sulfamoylphenyl derivative of indoline—A molecular dynamics study. *J. Mol. Model.* **2017**, *23*, 230. [[CrossRef](#)] [[PubMed](#)]
29. Lohith, T.N.; Hema, M.K.; Karthik, C.S.; Sandeep, S.; Mallesha, L.; Alsaiari, N.S.; Sridhar, M.A.; Katubi, K.M.; Abualnaja, K.M.; Lokanath, N.K.; et al. Persistent prevalence of non-covalent interaction in pyrimidine containing sulfonamide derivative: A quantum computational analysis. *J. Mol. Struct.* **2022**, *1266*, 133378. [[CrossRef](#)]
30. Contreras-García, J.; Yang, W.; Johnson, E.R. Analysis of hydrogen-bond interaction potentials from the electron density: Integration of noncovalent interaction regions. *J. Phys. Chem. A* **2011**, *115*, 12983–12990. [[CrossRef](#)]
31. Kasende, O.E.; Matondo, A.; Muzomwe, M.; Muya, J.T.; Scheiner, S. Interaction between temozolomide and water: Preferred binding sites. *Comput. Theor. Chem.* **2014**, *1034*, 26–31. [[CrossRef](#)]
32. Geerlings, P.; Fias, S.; Boisdenghien, Z.; De Proft, F. Conceptual DFT: Chemistry from the linear response function. *Chem. Soc. Rev.* **2014**, *43*, 4989–5008. [[CrossRef](#)]
33. Murray, J.S.; Politzer, P. The electrostatic potential: An overview, Wiley Interdiscip. *Rev. Comput. Mol. Sci.* **2011**, *1*, 153–163. [[CrossRef](#)]
34. Geerlings, P.; De Proft, F. Conceptual DFT: The chemical relevance of higher response functions. *Phys. Chem. Chem. Phys.* **2008**, *10*, 3028–3042. [[CrossRef](#)] [[PubMed](#)]
35. Liu, S.; Rong, C.; Lu, T. Information conservation principle determines electrophilicity, nucleophilicity, and regioselectivity. *J. Phys. Chem. A* **2014**, *118*, 3698–3704. [[CrossRef](#)] [[PubMed](#)]
36. Wang, B.; Rong, C.; Chattaraj, P.K.; Liu, S. A comparative study to predict regioselectivity, electrophilicity and nucleophilicity with Fukui function and Hirshfeld charge. *Theor. Chem. Acc.* **2019**, *138*, 124. [[CrossRef](#)]
37. Politzer, P.; Murray, J.S. Quantitative Analyses of Molecular Surface Electrostatic Potentials in Relation to Hydrogen Bonding and Co-Crystallization. *Cryst. Growth Des.* **2015**, *15*, 3767–3774. [[CrossRef](#)]
38. Isamura, B.K.; Lobb, K.A.; Muya, J.T. Regioselectivity, chemical bonding and physical nature of the interaction between imidazole and XAHs (X=H, F, Cl, Br, CH₃, and A=S, Se, Te). *Mol. Phys.* **2022**, *120*, e2026511. [[CrossRef](#)]
39. Isamura, B.K.; Patouossa, I.; Muya, J.T.; Lobb, K.A. Unveiling the reactivity of truxillic and truxinic acids (TXAs): Deprotonation, anion. . . H–O, cation. . . O and cation. . . π interactions in TXA⁰. . . Y⁺ and TXA⁰. . . Z[−] complexes (Y = Li, Na, K; Z = F, Cl, Br). *Struct. Chem.* **2022**, *34*, 97–112. [[CrossRef](#)]
40. Kumar, S.; Choudhary, M. Synthesis and characterization of novel copper(ii) complexes as potential drug candidates against SARS-CoV-2 main protease. *New J. Chem.* **2022**, *46*, 4911–4926. [[CrossRef](#)]

41. Cherrak, S.A.; Merzouk, H.; Mokhtari-Soulimane, N. Potential bioactive glycosylated flavonoids as SARS-CoV-2 main protease inhibitors: A molecular docking and simulation studies. *PLoS ONE* **2020**, *15*, e0240653. [[CrossRef](#)]
42. Mengist, H.M.; Dilnessa, T.; Jin, T. Structural Basis of Potential Inhibitors Targeting SARS-CoV-2 Main Protease. *Front. Chem.* **2021**, *9*, 622898. [[CrossRef](#)]
43. Zhang, L.; Lin, D.; Sun, X.; Curth, U.; Drosten, C.; Sauerhering, L.; Becker, S.; Rox, K.; Hilgenfeld, R. Crystal structure of SARS-CoV-2 main protease provides a basis for design of improved a-ketoamide inhibitors. *Science* **2020**, *368*, 409–412. [[CrossRef](#)] [[PubMed](#)]
44. Shin, D.; Mukherjee, R.; Grewe, D.; Bojkova, D.; Baek, K.; Bhattacharya, A.; Schulz, L.; Widera, M.; Mehdipour, A.R.; Tascher, G.; et al. Papain-like protease regulates SARS-CoV-2 viral spread and innate immunity. *Nature* **2020**, *587*, 657–662. [[CrossRef](#)] [[PubMed](#)]
45. Mohamed, M.E.; Tawfeek, N.; Elbaramawi, S.S.; Fikry, E. Agathis robusta Bark Essential Oil Effectiveness Against COVID-19: Chemical Composition, In Silico and In Vitro Approaches. *Plants* **2022**, *11*, 663. [[CrossRef](#)]

Disclaimer/Publisher’s Note: The statements, opinions and data contained in all publications are solely those of the individual author(s) and contributor(s) and not of MDPI and/or the editor(s). MDPI and/or the editor(s) disclaim responsibility for any injury to people or property resulting from any ideas, methods, instructions or products referred to in the content.